Strongly anisotropic spin relaxation in the neutral silicon vacancy center in diamond

B. C. Rose,[1] G. Thiering,[2,4] A. M. Tyryshkin,[1] A. M. Edmonds,[3] M. L. Markham,[3] A. Gali,[2,4] S. A. Lyon,[1] and N. P. de Leon[1,*]

[1]*Department of Electrical Engineering, Princeton University, Princeton, New Jersey 08544, USA*

[2]*Wigner Research Centre for Physics, Hungarian Academy of Sciences, P.O. Box 49, H-1525 Budapest, Hungary*

[3]*Element Six, Harwell OX11 0QR, United Kingdom*

[4]*Department of Atomic Physics, Budapest University of Technology and Economics, Budafokiút 8., H-1111 Budapest, Hungary*

(Received 10 October 2017; revised manuscript received 28 October 2018; published 20 December 2018)

Color centers in diamond are a promising platform for quantum technologies, and understanding their interactions with the environment is crucial for these applications. We report a study of spin-lattice relaxation (T_1) of the neutral charge state of the silicon vacancy center in diamond. Above 20 K, T_1 decreases rapidly with a temperature-dependence characteristic of an Orbach process and is strongly anisotropic with respect to magnetic-field orientation. As the angle of the magnetic field is rotated relative to the symmetry axis of the defect, T_1 is reduced by over three orders of magnitude. The electron spin coherence time (T_2) follows the same temperature dependence but is drastically shorter than T_1. We propose that these observations result from phonon-mediated transitions to a low-lying excited state that are spin conserving when the magnetic field is aligned with the defect axis, and we discuss likely candidates for this excited state.

DOI: 10.1103/PhysRevB.98.235140

I. INTRODUCTION

Solid-state defects are attractive candidates for quantum technologies because they can have long spin coherence time and can be integrated into nanofabricated devices. However, interactions with phonons can lead to spin decoherence. Color centers in diamond with exceptionally long spin coherence time have been identified, such as the nitrogen-vacancy center (NV^-), and these are promising candidates for a wide range of applications including quantum sensing [1], quantum information processing [2–5], and quantum networks [6–8]. More recently the negatively charged silicon vacancy center in diamond has been demonstrated to have better optical homogeneity but poor spin coherence at 4 K because of a phonon-mediated orbital relaxation process [9,10]. We recently demonstrated that the neutral charge state of the silicon vacancy center (SiV^0) can be implanted with high conversion efficiency, it exhibits excellent optical coherence with more than 90% of its emission into a nearly transform-limited zero-phonon line which does not exhibit any spectral diffusion, and it displays long spin coherence times at temperatures up to 20 K [11]. These properties make it an ideal candidate for a single atom quantum memory in a quantum network. However, we also observed that at temperatures above 20 K both T_1 and T_2 decrease exponentially with temperature [11,12]. Understanding the origin of this process is crucial for extending the operation range of SiV^0 to higher temperatures to enable new applications in quantum information processing and nanoscale sensing.

In this paper we investigate the spin-lattice relaxation of SiV^0 in detail. The exponential temperature dependence of T_1 above 20 K is consistent with an Orbach process [13–15] with an activation energy (E_a) of 16.8 meV, and we observe that the relaxation rate has a sharp dependence on the angle (θ) of the magnetic field ($\boldsymbol{B}$) relative to the symmetry axis of the defect [Fig. 1(a)]. As the angle of the magnetic field is rotated away from the crystallographic axis of SiV^0 by just 5°, T_1 decreases by almost two orders of magnitude. T_2 follows the same temperature dependence as T_1 but at a rate that is three orders of magnitude faster when the magnetic field is aligned with the defect symmetry axis.

We propose that the strong intrinsic anisotropy in the spin-lattice relaxation of SiV^0 and the significantly shorter spin coherence time originate from phonon-mediated transitions to an excited state that are spin conserving when the magnetic field is aligned with the quantization axis of the center. This is fundamentally similar to previous observations in SiV^- at 4 K in which a fast orbital relaxation ($T_{1,\mathrm{orbital}} = 38$ ns) is spin conserving but spin dephasing, giving rise to a relatively long $T_{1,\mathrm{spin}} = 2$ ms, whereas T_2 is limited by the orbital relaxation rate [9,16]. For SiV^-, spin relaxation arises from differing spin-orbit coupling in the two low-lying orbital states, and when the external magnetic field is aligned with the SiV^- axis, this spin relaxation is suppressed, leading to $T_{1,\mathrm{spin}} \gg T_{1,\mathrm{orbital}}$. However, in a large off-axis magnetic field, the eigenstates mix, and the spin-relaxation rate increases rapidly with the angle θ [16].

The identity of the state at 16.8 meV implied by the activation energy is unknown. Likely candidates are a low-lying singlet state or a triplet vibronic mode [17]. For both candidates, we develop models that explain the observed suppression of spin relaxation when the magnetic field is aligned with the quantization axis, the temperature and orientation dependence of T_1, and the ratio between T_1 and T_2. We show that a model incorporating a singlet excited state closely reproduces our data, and we outline the physical requirements for a triplet excited state that would account for the observations.

*npdeleon@princeton.edu

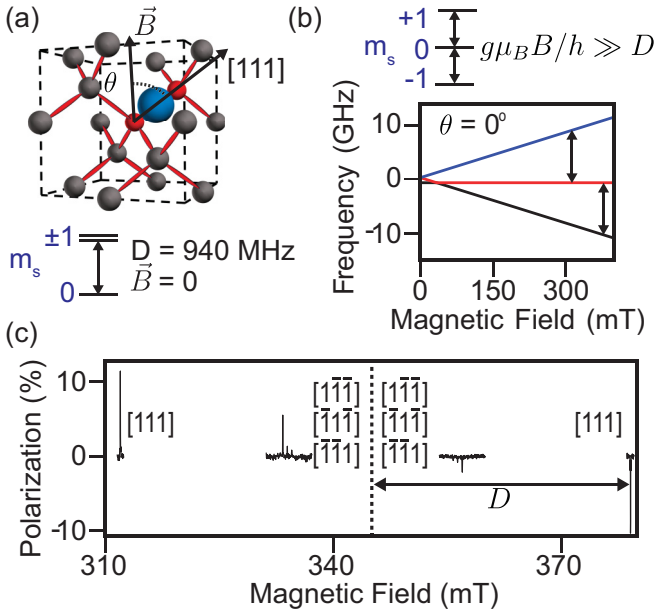

FIG. 1. [(a), top] Ball and stick model of SiV^0. Gray spheres are carbon atoms. The interstitial Si atom (blue sphere) and split vacancy (red spheres) are aligned along the ⟨111⟩ directions in the diamond lattice, and the magnetic field ($\boldsymbol{B}$) forms angle θ with the defect axis. [(a), bottom] Ground-state SiV^0 spin levels at $\boldsymbol{B} = 0$. [(b), top] Ground-state spin levels at magnetic fields such that the Zeeman energy is high compared to the zero-field splitting $g\mu_B \boldsymbol{B}/h \gg \mathbf{D}$. [(b), bottom] Magnetic-field dependence of spin levels with $\boldsymbol{B} \parallel$ [111]. Arrows indicate the magnetic field required for each spin transition to match the 9.7 GHz resonator mode. (c) Pulsed electron spin resonance (ESR) spectrum of SiV^0 (zero-field splitting, $D =$ 0.94 GHz or 33.5 mT) measured at X-band frequency (9.7 GHz) with the magnetic field slightly misaligned from [111] by $\theta = 2.6°$. Four sets of peaks correspond to $m_s = 0 \leftrightarrow +1$ and $m_s = -1 \leftrightarrow 0$ transitions for two inequivalent orientations.

II. METHODS

Two high-purity {110} diamonds grown by chemical vapor deposition were studied. The first diamond (D1) was doped during growth with boron ($\gtrsim 10^{17}$ cm^{-3}) and silicon ($\sim 10^{17}$ cm^{-3}) and subsequently high-pressure–high-temperature annealed, resulting in a SiV^0 concentration of 4×10^{16} cm^{-3} [18]. The silicon precursor was isotopically enriched with 90% ^{29}Si, and all measurements in D1 were conducted on a ^{29}Si hyperfine line. The second diamond (D2) was doped during growth with boron ($\sim 10^{17}$ cm^{-3}) and implanted with ^{28}Si (6.3×10^{15} cm^{-3}) and was previously described in Ref. [11]. After implantation and annealing, the resulting SiV^0 concentration was 5.1×10^{15} cm^{-3} within the implanted region. Pulsed X-band (9.7-GHz) ESR was performed in a dielectric volume resonator (Bruker MD5) with a quality factor of 5000 (see Appendix A) [19]. In all experiments the microwave power was chosen so that the excitation pulse bandwidth was greater than the bulk linewidth of spin transitions (∼1 MHz). T_2 was measured using a standard two-pulse Hahn echo sequence with an initial 100-ms green laser pulse (532 nm, 200 mW) to optically enhance the spin polarization. At 5 K, we achieve 11.5% optical spin polarization into $m_s = 0$ [Fig. 1(c)]. T_1 was measured using a three-pulse inversion recovery sequence [20].

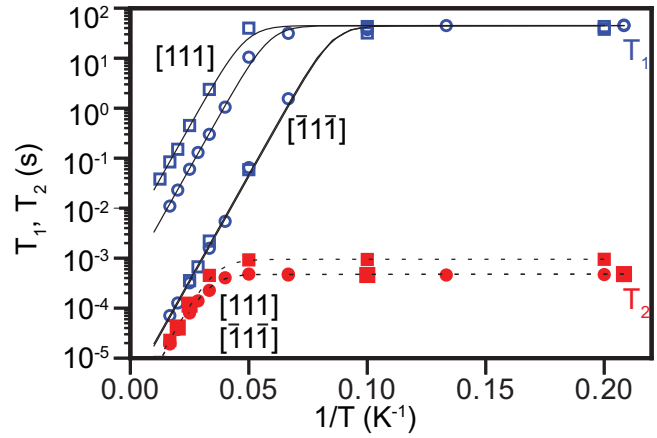

FIG. 2. Arrhenius plot of the temperature dependence of T_1 (blue) and T_2 (red) for SiV^0 in D1 (circles) and D2 (squares) for two inequivalent orientations with $\boldsymbol{B} \parallel$ [111]. [111]: $\theta = 2.6°$ (D1), $\theta = 0.8°$ (D2), and [$\bar{1}\bar{1}$1]: $\theta = 106.9°$ (D1), $\theta = 108.7°$ (D2). Lines correspond to the best fit of Eq. (2).

III. RESULTS

A. Temperature dependence of T_1 and T_2

The ground-state spin Hamiltonian is given by [18]

$$\hat{H} = \hat{\boldsymbol{S}}^\dagger \tilde{D}_g \hat{\boldsymbol{S}} + \mu_B \hat{\boldsymbol{S}}^\dagger \tilde{g} \boldsymbol{B}, \tag{1}$$

with electron spin $S = 1$, zero-field splitting tensor ($\tilde{D}_g$) with axial part $D_g = 0.94$ GHz (at $T = 4.8$ K), electron g tensor ($\tilde{g}$) with parallel and perpendicular components $g_\parallel = 2.0042$ and $g_\perp = 2.0035$, respectively, and the Bohr magneton μ_B. The $\tilde{D}$ and $\tilde{g}$ tensors are both aligned along the ⟨111⟩ directions. With the field aligned along [111], there are two inequivalent orientations [Fig. 1(c)]: One orientation aligned with the field, $\theta = 0°$ ([111], outer ESR peaks), and three equivalent orientations aligned off axis, $\theta = 109.5°$ ([$\bar{1}\bar{1}$1], [1$\bar{1}$1], [$\bar{1}$11], inner ESR peaks).

We performed time-resolved measurements of spin relaxation and decoherence for both inequivalent orientations. At low temperatures, T_1 and T_2 are constant (Fig. 2). In sample D2, we previously reported that the SiV^0 low-temperature T_2 is dominated by spectral diffusion from the 1.1% abundance of ^{13}C nuclei, $T_2 = 0.954 \pm 0.025$ ms [11]. By contrast, the SiV^0 density in D1 is large enough that T_2 is limited by instantaneous diffusion, $T_2 = 0.48 \pm 0.03$ ms (see Appendices B and C) [21]. At low temperatures, T_1 is constant, $T_1 = 46 \pm 2$ s (D1), and $T_1 = 45 \pm 4$ s (D2), similar to previous observations of NV^- [22].

Above 20 K, both T_1 and T_2 decrease exponentially with increasing temperature. In this regime the two inequivalent orientations exhibit similar T_2 but significantly different T_1's, T_1 and T_2 exhibit the same Arrhenius slope (the slope of the logarithm of the rate vs inverse temperature) for both orientations. The data ($T_{1,[111]}$, $T_{1,[\bar{1}\bar{1}1]}$, $T_{2,[111]}$, $T_{2,[\bar{1}\bar{1}1]}$) were

TABLE I. Summary of the rate prefactors $A_{T_1,T_2}(\theta)$ extracted from fitting the curves in Fig. 2.

Sample	$A_{T_1}(\theta = 0°)$ (10^3 s^{-1})	$A_{T_1}(\theta = 109°)$ (10^3 s^{-1})	$A_{T_2}(\theta = 0°, 109°)$ (10^3 s^{-1})
D1	2.10 ± 0.28	378 ± 33	1260 ± 152
D2	0.3 ± 0.02	365 ± 53	1180 ± 210

fit according to the equation,

$$\frac{1}{T_{1,2}} = \frac{1}{T_{\text{sat}}} + A_{T_1,T_2}(\theta)e^{-E_a/kT}, \tag{2}$$

where T_{sat} is the saturated decay time at low temperatures, $A_{T_1,T_2}(\theta)$ is the orientation-dependent rate prefactor, E_a is the activation energy, and kT is the thermal energy. $E_a = 16.8 \pm 1.5$ meV for all curves, but $A_{T_1,T_2}(\theta)$ varies significantly (Table I).

Unlike T_1, T_2 exhibits a weak orientation dependence. However, since T_2 displays the same activation energy as T_1, the two decay times likely result from the same physical process. This is surprising since T_2 is not T_1 limited; T_2 is 4000 times shorter than T_1 when $\theta = 0°$. We can rule out that the decoherence is caused by magnetic noise from nearby centers because we do not observe a density dependence in T_2 when comparing samples D1 and D2, and we are unable to extend T_2 with further dynamical decoupling (see Appendix D) [11]. Moreover, numerical simulations of ensemble dipolar interactions fail to account for the observed temperature dependence of T_2 (see Appendix C).

B. Orientation dependence of T_1 and T_2

We measured the detailed orientation dependence of T_1 and T_2 at 30 K (Fig. 3) where the Orbach process dominates spin relaxation. At a magnetic field of ∼340 mT [Fig. 1(b)], the Zeeman frequency (9.7 GHz) is much larger than the zero-field splitting (0.94 GHz). The relative orientation of the field was varied by rotating the crystal about a ⟨110⟩ axis from $\theta = 0°$ ($\boldsymbol{B} \parallel \boldsymbol{D}$) to $\theta = 90°$ ($\boldsymbol{B} \perp \boldsymbol{D}$). The ESR spectrum [Fig. 1(c)] was measured to determine orientation to within 1°. The relaxation time exhibits dramatic anisotropy, and as the crystal is rotated away from $\theta = 0°$, spin relaxation becomes clearly biexponential (Fig. 3). Near $\theta = 0°$, T_1 drops rapidly, and rotating by just 5° increases the relaxation rate by almost two orders of magnitude. Near $\theta = 55°$, the decay is a single exponential with a short timescale that is insensitive to small rotations. Beyond 55° the two timescales diverge differing by over 3 orders of magnitude at $\theta = 90°$ [Fig. 3(b)].

C. Model for the Orbach process

We propose a model that captures the four salient features of the data: (1) the strong anisotropy of T_1, (2) the biexponential nature of T_1, (3) the temperature dependence of T_2, and (4) the large ratio between T_1 and T_2. Generically, an Orbach process is a two-phonon process [15] that connects the ground-state spin sublevels $m_s = -1, 0, +1$ through an excited state ($|\Psi\rangle$) with amplitudes t_{-1}, t_0, and t_{+1}, respectively [Fig. 4(a)]. The amplitudes (t_{-1}, t_0, and t_{+1}) are overlap

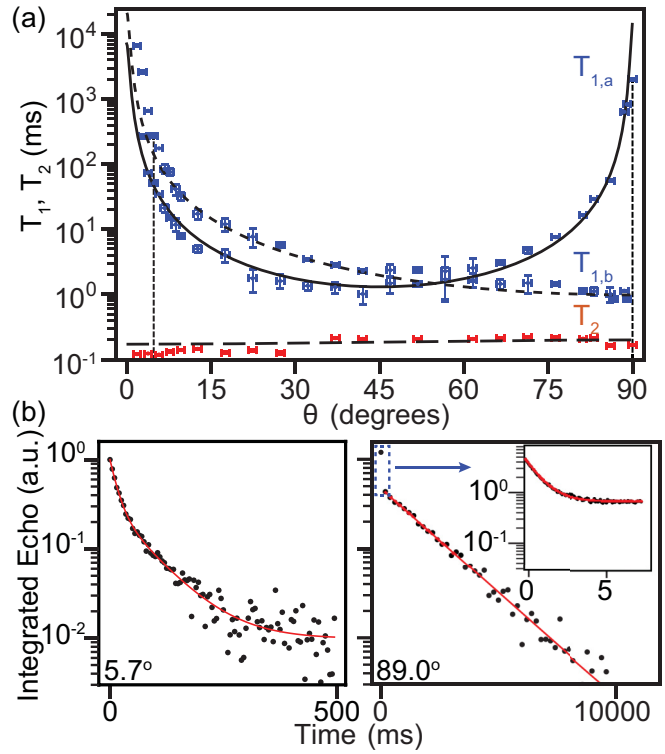

FIG. 3. (a) Orientation dependence of T_1 (blue dots) and T_2 (red dots) in sample D1 at $T = 30$ K, measured on the $m_s = 0 \leftrightarrow +1$ transition. Lines show the theoretical orientation dependence of the two characteristic spin-relaxation times $T_{1,a}$ (solid line), $T_{1,b}$ (dashed line), and T_2 (long dashed line) for an Orbach process with an excited singlet state. (b) Selected decay curves with their corresponding fits (red) showing the biexponential behavior of T_1 at particular orientations (θ), indicated by vertical dashed lines in (a). The dashed box indicates the region where an additional measurement was performed with finer time resolution, shown in the inset.

parameters between the ground triplet states and the excited-state $t_{m_s} = \langle m_s|\Psi\rangle$ (see Appendices G and H). This gives rise to three possible relaxation rates between pairs of ground-state spin sublevels $m_s \leftrightarrow m_{s'} = -1 \leftrightarrow 0,\ 0 \leftrightarrow +1,\ -1 \leftrightarrow +1$,

$$\frac{1}{T_{1,m_s \leftrightarrow m_{s'}}} = C|t_{m_s}t_{m_{s'}}|^2 e^{-E_a/kT}, \tag{3}$$

where C is a constant.

If the excited-state Ψ is a singlet ($S = 0$), it is invariant under magnetic-field orientation, so the behavior of T_1 can be captured by considering the mixing of the ground state (see Appendix G). The mixing of the spin sublevels in the presence of a large off-axis magnetic field leads to

$$\begin{pmatrix} |t_{-1}|^2 \\ |t_0|^2 \\ |t_{+1}|^2 \end{pmatrix} = \begin{pmatrix} \cos^4\frac{\theta}{2} & \frac{1}{2}\sin^2\theta & \sin^4\frac{\theta}{2} \\ \frac{1}{2}\sin^2\theta & \cos^2\theta & \frac{1}{2}\sin^2\theta \\ \sin^4\frac{\theta}{2} & \frac{1}{2}\sin^2\theta & \cos^4\frac{\theta}{2} \end{pmatrix} \begin{pmatrix} |t^0_{-1}|^2 \\ |t^0_0|^2 \\ |t^0_{+1}|^2 \end{pmatrix}, \tag{4}$$

where $|t^0_{m_s}|^2$ are the overlap parameters at zero magnetic field. Substituting Eq. (4) in Eq. (3) and solving the 3×3 relaxation rate matrix equation for the ground-state spin ($S = 1$) provides the T_1 relaxation times (see Appendix G). If $|t^0_0| = |t^0_{-1}| = |t^0_{+1}|$, then Eqs. (3) and (4) predict that the

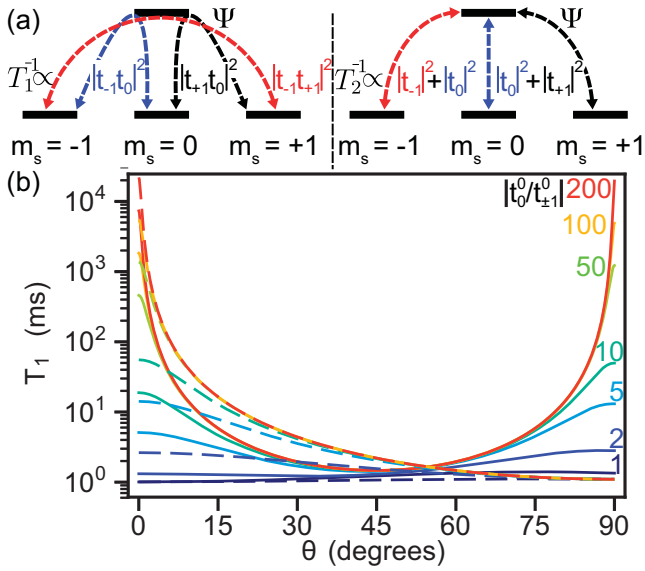

FIG. 4. (a) Level diagram of the Orbach process with a singlet excited state. Spin relaxation (left) occurs in two steps through the excited state and depends on the product of the overlap parameters, whereas decoherence (right) can arise from a single step and depends on the sum. (b) Plot of $T_{1,a}$ (solid curves) and $T_{1,b}$ (dashed curves) for selected values of $|t_0^0/t_{\pm1}^0|$ using the extracted rate coefficient C.

spin relaxation is isotropic. However, if $|t_0^0| \gg |t_{-1}^0|, |t_{+1}^0|$, the spin relaxation is strongly anisotropic with two characteristic times approximated as

$$\frac{1}{T_{1,a}} = \frac{3}{8} C \left|t_0^0\right|^4 \sin^2(2\theta) e^{-E_a/kT},$$
$$\frac{1}{T_{1,b}} = \frac{1}{2} C \left|t_0^0\right|^4 \sin^2(\theta) e^{-E_a/kT}. \quad (5)$$

In this limit the model captures the observed angular dependence of the two timescales in T_1 [Fig. 3(a)]. By comparing numerical calculations of the orientation dependence of T_1 for different ratios of $|t_0^0/t_{\pm1}^0|$ [Fig. 4(b)], we can place a lower bound on the imbalance between these rates $|t_0^0/t_{\pm1}^0| > 100$.

We can also predict the effect of this Orbach process on T_2. Customarily, the Orbach process is viewed as a spin-relaxation process [15]. However, phonon-mediated transitions to the excited state can also lead to decoherence even when the spin projection is preserved, similar to what has been observed for orbital relaxation in SiV^- [16]. Although the spin-relaxation rate relies on a spin flip and therefore the product of the overlap parameters $\frac{1}{T_1} \propto |t_{m_s}|^2 |t_{m_{s'}}|^2$ [Fig. 4(a), left], the decoherence rate depends on the sum of overlap parameters $\frac{1}{T_2} \propto |t_{m_s}|^2 + |t_{m_{s'}}|^2$ [Fig. 4(a), right] if we assume the spin coherence is completely lost after a single excitation to the excited state Ψ. The angle-dependent ratio of T_1 to T_2 will therefore depend on the ratio of overlap parameters. The model predicts (Fig. 9)

$$\frac{T_{1,a}}{T_{2,0\leftrightarrow\pm1}} = \frac{(|t_{\pm1}|^2 + |t_0|^2)\left(|t_0^0|^2 + 2|t_{\pm1}^0|^2\right)}{3|t_{\pm1}t_0|^2}. \quad (6)$$

The orientation dependence of T_2 predicted from this model is plotted in Fig. 3(a) where we also included the effect of instantaneous diffusion in sample D1 and is plotted in detail in Fig. 11. The anisotropy in T_2 is mostly canceled in the sum $|t_{m_s}|^2 + |t_{m_{s'}}|^2$. The model provides the best fit for both the T_1 and the T_2 data when $|t_0^0/t_{\pm1}^0| \approx 125$ [Fig. 3(a)].

If excited-state Ψ is instead a triplet ($S = 1$), the overlap parameters cannot be written compactly, but we analyze this case numerically (see Appendix H). Briefly, phonon-mediated orbital relaxation to a vibronic excited state is generally spin conserving, but differences in the ground- and excited-state spin Hamiltonians can lead to mixing during the time spent in the excited state. For SiV^0 the ground and excited states can have different zero-field splitting tensors (D_e and D_g). Since the Zeeman splitting in these measurements is 9.7 GHz, the zero-field splittings must differ by a comparable scale in order to reproduce the observed ratio of T_1 to T_2, and we find that the data can be qualitatively reproduced when $D_e \sim$ 5–7 GHz [Figs. 6 and 7(b)], compared to the ground-state zero-field splitting $D_g = 0.94$ GHz. It is unlikely that the zero-field splittings differ by such a large magnitude. Alternatively, the small ratio of T_1 to T_2 could also arise from incomplete spin dephasing. If the excited-state lifetime is short compared to the spin precession time ($\tau < \pi\hbar/E_{\text{Zeeman}} \sim 50$ ps), then the spin coherence is partially preserved through a single excitation to Ψ [23]. A model involving a triplet excited state would therefore require either that $D_e \gg D_g$ or that the excited-state lifetime is short enough to partially preserve coherence.

IV. CONCLUSIONS

To summarize, we have shown that spin relaxation in SiV^0 at high temperatures is dominated by an Orbach process that is strongly dependent on the magnetic-field orientation and T_2 exhibits the same temperature dependence as T_1 but at a significantly faster rate. These observations can be explained by a model for the Orbach process where the overlap parameters from the $m_s = 0$ and $m_s = \pm1$ spin sublevels to a singlet excited state are drastically different. We note that this is consistent with the preferential optical spin polarization through the intersystem crossing into $m_s = 0$ [Fig. 1(c)] [11]. Alternatively, these observations can be qualitatively reproduced by a model with a triplet excited state that either exhibits a much larger zero-field splitting than the ground state or a very short excited-state lifetime. Although our present results cannot definitively identify the excited state, detailed spectroscopy can help distinguish between these two cases. Absorption spectroscopy could elucidate the vibronic structure [24,25], and the nature of the singlet state can be explored using time-resolved photon correlation measurements and temperature-dependent intersystem crossing rates [26,27]. At temperatures well above the activation energy, there should be enough population in the excited state to observe spin-resonance transitions associated with a different zero-field splitting. We have not observed the existence of additional transitions, but on-going work includes increasing our sensitivity at higher temperatures to search for such states.

The strong intrinsic anisotropy in SiV^0 stands in contrast to prior studies of NV^- in which spin relaxation is mostly insensitive to the magnetic-field orientation at low magnetic field (5 mT) [28]. Our work suggests that it would be interesting to perform measurements of the orientation

and temperature dependence of spin relaxation in NV^- at high magnetic fields. Similarly, a more detailed orientation and temperature dependence of $T_{1,\mathrm{spin}}$ in SiV^- would further elucidate analogous spin- and orbital-relaxation processes, and recent measurements at dilution refrigerator temperatures have started to explore mechanisms for spin relaxation and decoherence [29,30].

These observations point to a particularly intriguing possibility for high-temperature operation if Ψ is a spin singlet. The small overlap parameters between $m_s = \pm 1$ and Ψ imply that superpositions of $m_s = \pm 1$ could have longer spin coherence time than even the measured single-quantum T_1 as they should be limited instead by the double-quantum T_1 (see Appendix J). Future experiments include double-quantum spin resonance to interrogate the coherence of such superposition states [31].

ACKNOWLEDGMENTS

This work was supported by the Princeton Center for Complex Materials, an NSF MRSEC (Grant No. DMR-1420541) and the NSF EFRI ACQUIRE Program (Program No. 1640959). G.T. and A.G. were supported by the NKP-17-3-III New National Excellence Program of the Ministry of Human Capacities and the EU Commission (ASTERIQS Contract No. 820394). The authors gratefully acknowledge J. Thompson, S. Kolkowitz, and A. Ajoy for helpful discussions, as well as S. Sangtawesin and Z. Zhang for help in proofreading the paper.

APPENDIX A: EXPERIMENTAL DETAILS

Electron spin resonance was performed on a modified Bruker Elexsys 580 system with a 1.4-T electromagnet [Fig. 5(a)]. This is performed by driving the TE011 mode of a cylindrical dielectric resonator (ER-4118X-MD5) (9.7 GHz) with an external vector microwave source (Agilent E8267D). Temperature-dependent measurements were performed in an Oxford CF935 helium-flow cryostat. The microwave excitation channel consists of a vector microwave source (Agilent, E8267D), a variable gain solid-state amplifier (AR 20S4G11), a protection *p-i-n* diode (Hittite switch), and a variable attenuator (ARRA P4844-30). This allows for arbitrary waveform control as well as flexibility in the microwave power delivered to the resonator which is necessary for handling the range of quality factors and excitation bandwidths needed across several samples. The microwave excitation is coupled capacitively to the resonator through a microwave waveguide terminated with an open-loop antenna, and the reflected microwaves are returned through a fast Hittite switch (HMC547) redirecting the microwaves to the detection channel. The reflected microwave signal is sent through a cryogenic low noise amplifier (Low Noise Factory, LNF-LNC4_16B) and then through a room-temperature low noise amplifier (Bruker). To avoid saturating and damaging the cryogenic amplifier, it must be protected from the microwave excitation during the ring-down period of the resonator. This protection was supplied by the fast Hittite microwave switch, which was used to couple the reflected microwave excitation out of the resonator back to the excitation pathway. After the ring-down period the switch is opened up to the cryogenic amplifier so that any spin signal outside of the ring-down period is amplified. The amplified signal is sent to a quadrature detector (Bruker) where it is mixed with a reference signal from the vector source. The in-phase (I) and quadrature (Q) signals coming out of the mixer are read with a fast digitizing board (Bruker SpecJet). Triggering in this experiment was controlled with a PulseBlaster ESR-PRO board.

Spin coherence measurements (T_2) were performed using a two-pulse Hahn echo sequence with an initial laser pulse to boost the echo strength by polarizing the spins preferentially into $m_s = 0$ [Fig. 5(b)]. Spin-relaxation measurements (T_1) were performed using a three-pulse inversion recovery sequence [Fig. 5(b)]. First a laser pulse is used to polarize the SiV^0 spins preferentially into $m_s = 0$. After a small delay to wait for any laser-induced noise to die out, a microwave π pulse is applied to invert the spin polarization even further away from the Boltzmann equilibrium. The waiting time in this inverted state (T) is varied, and a two-pulse Hahn echo sequence ($\pi/2 - \tau - \pi - \tau$ echo) is used to read out the polarization at the end of the waiting period. For the strongest signal τ is chosen to be much smaller than T_2.

APPENDIX B: INSTANTANEOUS DIFFUSION IN SAMPLE D1

At low temperatures, the coherence time in sample D1 is limited by instantaneous diffusion, which arises when a microwave pulse induces spin flips on a dense bath of paramagnetic centers. If we consider a central spin surrounded by its neighbors, then the pulse will induce rotations of the neighbors as well as the central spin. The phase resulting from the pulse-induced change in the dipolar magnetic field from the neighbors is not refocused during a Hahn echo sequence, limiting the coherence time of the central spin to $T_{2(ID)}$ [32].

The effect of instantaneous diffusion can be mitigated by using a smaller rotation angle (θ_2) for the second microwave pulse of a Hahn echo sequence since the change in the net dipolar magnetic field scales as $\sin^2(\theta_2/2)$. This results in a proportionally smaller phase accumulated by the central spin and a decoherence rate $1/T_2 \propto T_{2(ID)}^{-1} \sin^2(\theta_2/2)$. Using a smaller rotating angle will enhance T_2, but it will also decrease the bulk echo signal by the same factor. In sample D1, the apparent decoherence rate increases linearly with $\sin^2(\theta_2/2)$ (Fig. 6). The data were fit according to the following:

$$\frac{1}{T_2} = \frac{1}{T_{2(SD)}} + \frac{1}{T_{2(ID)}} \sin^2(\theta_2/2), \tag{B1}$$

where $T_{2(SD)}$ is the spectral diffusion decay time. The fit results in $T_{2(SD)} = 0.95 \pm 0.22$ ms, most likely arising from the 1.1% of the ^{13}C nuclei [11] and $T_{2(ID)} = 0.319 \pm 0.056$ ms.

We note that the Hahn echo spin coherence times reported for sample D1 in Figs. 6, 10(c), and 11 ($T_2 = 0.28$ ms) is not the same as the spin coherence time reported in Fig. 2 in the main text ($T_2 = 0.48$ ms). This arises from the nonuniform population distribution of SiV^0 centers in this sample over the four inequivalent crystal orientations ([111], $[1\bar{1}\bar{1}]$, $[\bar{1}1\bar{1}]$, $[\bar{1}\bar{1}1]$), which has been reported previously as sample C in Ref. [33]. The data in Figs. 3, 8, 10,

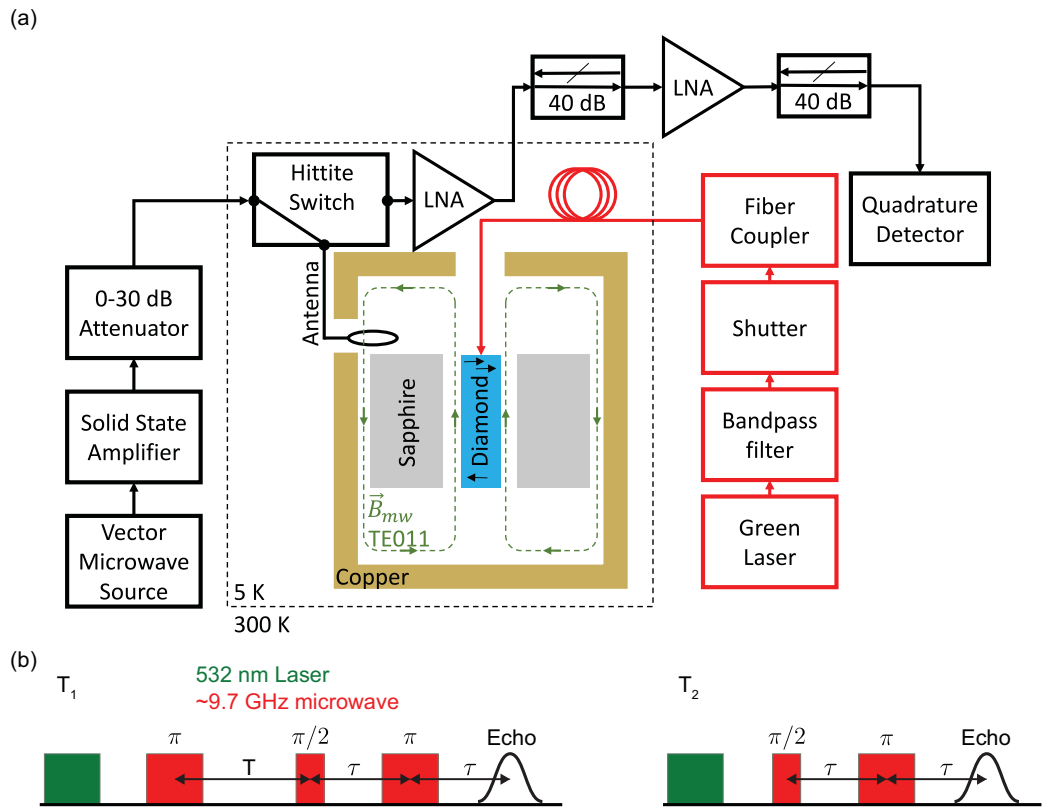

FIG. 5. (a) Electron spin-resonance setup. (b) Experimental pulse sequence for bulk electron spin-resonance measurements of T_1 and T_2. A vector microwave source is amplified and coupled capacitively to the TE011 mode of a sapphire-dielectric cylindrical resonator. The diamond sample sits in the center of the resonator where the microwave field (B_{mw}) is uniform. The spin echo is coupled out of the resonator through a different path set by a fast Hittite microwave switch and amplified by a low-noise cryogenic preamplifier. Optical excitation from a green laser (532 nm) is controlled with a mechanical shutter and fiber coupled to the sample.

11, and 6 are taken using the $[\bar{1}1\bar{1}]$ orientation (larger SiV^0 concentration), whereas the data in Fig. 2 are taken using the [111] orientation (smaller SiV^0 concentration).

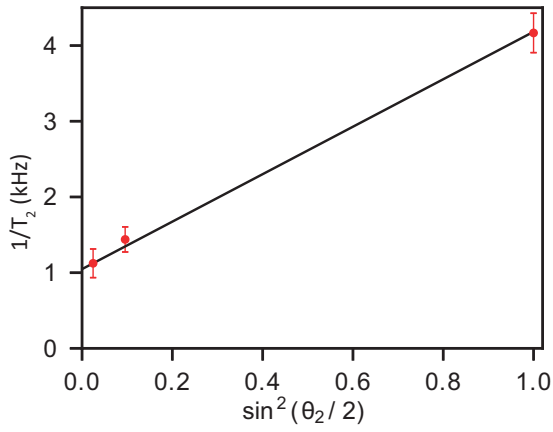

FIG. 6. Decoherence rates for SiV^0 centers in sample D1 measured at 5 K as a function of the rotation angle (θ_2) of the second pulse in a Hahn echo sequence. The linear dependence confirms that T_2 is limited by instantaneous diffusion. The black curve is a fit according to Eq. (B1).

APPENDIX C: DECOHERENCE ARISING FROM T_1-INDUCED SPIN FLIPS OF FAST RELAXING NEIGHBORS

An alternative hypothesis for the observed temperature dependence of T_2 (Fig. 2 in the main text) and its relative magnitude with respect to T_1 is that rapid dephasing arises from dipolar interactions with other SiV^0 spins in the bath, such as those misaligned with the external magnetic field. We can immediately rule out spectral diffusion from SiV^0 spin flip-flops and instantaneous diffusion mechanisms arising from dipolar interactions between SiV^0 centers since these mechanisms would be independent of temperature. Instead, we consider the contribution of spectral diffusion arising from the fast T_1 relaxation of nearby SiV^0 centers [34]. This decoherence mechanism is strongest when T_1 of the spin bath is comparable to T_2 of the central spin under consideration.

In our samples, $T_2 \sim 0.5$ ms at low temperatures, which is comparable to $T_1 \sim 1$ ms of the three equivalent SiV^0 orientations misaligned with the magnetic field ($\theta \approx 109^\circ$) at temperatures above 20 K. We numerically model the contribution to the Hahn echo decay from these three equivalent off-axis sites for the range of densities in samples D1 and D2 [35]. The electron spin Hamiltonian describing a pair of SiV^0 spins S_1 and S_2 is given by

$$\hat{H} = \hbar\omega_1 \hat{S}_{1z} + \hbar\omega_2 \hat{S}_{2z} + \hbar A(\boldsymbol{r}_{12}) \hat{S}_{1z} \hat{S}_{2z} + \hat{V}_2(t), \quad \text{(C1)}$$

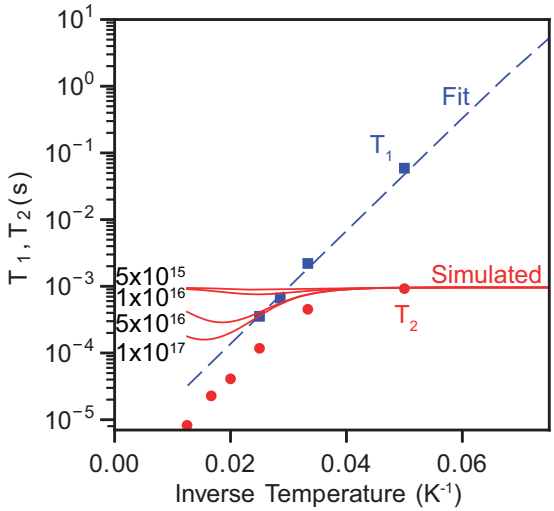

FIG. 7. Arrenhius plot of simulations of T_2 (red lines) resulting from spectral diffusion arising from fast relaxing SiV^0 centers. The blue dashed line is a fit of Eq. (2) to the temperature dependence of T_1 (blue squares) of fast relaxing SiV^0 sites. This fit is incorporated in Eq. (C3) to simulate T_2 for a range of defect densities (labels in units of cm^{-3}). The simulations indicate that, for the range of densities studied, the decoherence arising from spin flips of nearby SiV^0 centers is not significant and is inconsistent with the observed temperature dependence of T_2 (red dots).

with dipolar interaction between the SiV^0 spins,

$$A(\boldsymbol{r}_{12}) = g_{1z}g_{2z}\mu_B^2\hbar^{-1}[1 - 3\cos^2(\theta_{12})]r_{12}^{-3}, \qquad \text{(C2)}$$

where ω_1 and ω_2 are the transition frequencies of the spins, r_{12} is the distance between the spins, θ_{12} is the angle between $\boldsymbol{r}_{12}$ and $\boldsymbol{B}$, and g_{1z} and g_{2z} are the longitudinal components of the g tensors. For our model we consider that S_1 is a slow relaxing spin ($\theta = 0°$) whose coherence time is being measured and S_2 is a fast relaxing spin ($\theta = 109°$) whose spontaneous T_1 flips induce decoherence of S_1. The term $\hat{V}_2(t)$ accounts for the fast Orbach spin-relaxation rate of S_2 spins by inducing random spin flips at a rate W. The contribution to the echo signal decay for S_1 is [35] as follows:

$$V(2\tau) = \left[\left(\cosh(R\tau) + \frac{W}{R}\sinh(R\tau)\right)^2 + \frac{A^2(\boldsymbol{r}_{12})}{4R^2}\sinh(R\tau)\right]\exp(-2W\tau), \qquad \text{(C3)}$$

where τ is the interpulse delay in a Hahn echo sequence, $W = 1/T_{1,\langle\bar{1}1\bar{1}\rangle}$ (fast relaxing sites, Fig. 7 blue line), $R^2 = W^2 - A^2(\boldsymbol{r_{12}})/4$, and $r_{12} = n^{-1/3}$ is the average interspin distance. This expression is averaged over all angles θ_{12} and added to the Hahn echo decay that arises from ^{13}C spectral diffusion alone ($T_{2(SD)} = 0.95$ ms). The resulting calculated Hahn echo decay times are shown in Fig. 7 for several SiV^0 densities in and above the range of the two samples studied here, which have SiV^0 concentrations of less than 5×10^{16} cm^{-3}. The density required to account for the data would need to be 100 times higher. Furthermore, at high temperatures, motional narrowing should lead to an increase in T_2, which does not qualitatively agree with the observed temperature dependence (Figs. 2 and 7).

APPENDIX D: DYNAMICAL DECOUPLING USING THE CARR-PURCELL-MEIBOOM-GILL SEQUENCE

We previously reported dynamical decoupling measurements using the Carr-Purcell-Meiboom-Gill (CPMG) sequence on sample D2 [11,36]. The Hahn echo T_2 displays a plateau below 20 K corresponding to ^{13}C spectral diffusion but is limited by an Orbach process above 20 K. We observed that $T_{2,\mathrm{CPMG}}$ is unchanged above 20 K and follows the temperature dependence of T_2. However below 20 K $T_{2,\mathrm{CPMG}}$ becomes substantially longer than T_2 and follows the extrapolated temperature dependence of the Orbach process. We hypothesize that the CPMG experiment refocuses slow spectral diffusion that arises from the ^{13}C nuclei, but it does not refocus fast effects from the Orbach process as expected. All of the points in the CPMG measurement lie along the same curve $T_{2,\mathrm{CPMG}}^{-1} = A\exp(-E_a/kT)$, where $A = 1180 \pm 210$ kHz and $E_a = 16.8 \pm 1.5$ meV in the entire measured temperature range of 5–60 K.

APPENDIX E: ORIENTATION DEPENDENCE OF T_1 AND T_2 MEASURED ON $m_s = -1 \leftrightarrow 0$

In the main text we presented the orientation dependence of the T_1 and T_2 times for SiV^0 for measurements on the $m_s = 0 \leftrightarrow +1$ transition. We also repeated the same measurements on the $m_s = -1 \leftrightarrow 0$ transition and find that it gives a nearly identical orientation dependence (Fig. 8). Since $T_{1,-1\leftrightarrow 0} \approx T_{1,0\leftrightarrow 1}$, we can conclude that $|t_{+1}^0| \approx |t_{-1}^0|$. Additionally, because of the 1-GHz zero-field splitting of SiV^0, the measurements on the $m_s = -1 \leftrightarrow 0$ transition were performed at a field that was ~30 mT larger (when aligned with the [111] direction) compared to the measurements on the $m_s = 0 \leftrightarrow +1$ transition in Fig. 3. This implies that the Orbach process has a weak dependence on the magnetic-field strength.

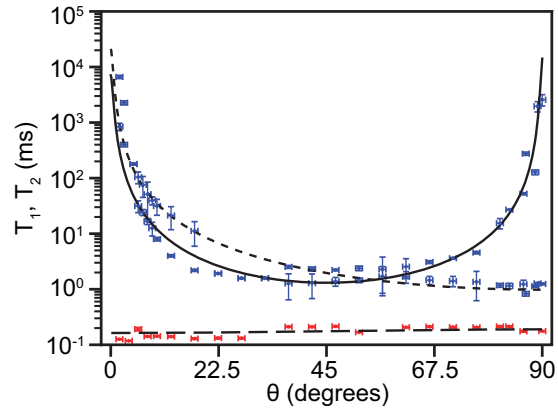

FIG. 8. Orientation dependence of T_1 (blue) and T_2 (red) measured at 30 K on the $m_s = -1 \leftrightarrow 0$ transition. The lines were simulated for the Orbach model with a singlet excited state using Eq. (G12) and assuming $|t_0^0/t_{\pm 1}^0| = 125$: (solid line) $T_{1,a}$, (dashed line) $T_{1,b}$, and (long dashed line) T_2.

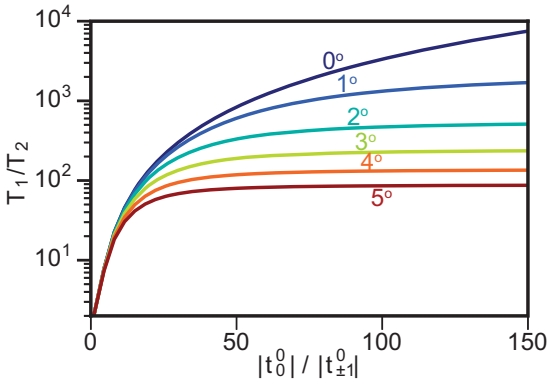

FIG. 9. Plot of $T_{1,a}/T_{2,0\leftrightarrow\pm1}$ vs $|t_0^0|/|t_{\pm1}^0|$ from Eqs. (5) and (6) for several values of θ.

APPENDIX F: RATIO OF T_1 TO T_2

The singlet model predicts that the observed ratio of T_1 to T_2 in Figs. 2 and 3 is strongly dependent on the ratio of the overlap parameters at zero field. The analytical form of this dependence is shown in Eqs. (5) and (6) which is plotted in Fig. 9. This figure shows that this ratio is strongly dependent on the orientation of the magnetic field, indicating that the best way to extract the ratio of the zero-field overlap parameters is by performing a global fit across all orientations (Fig. 3).

APPENDIX G: MODEL FOR SPIN RELAXATION: ORBACH PROCESS WITH A SINGLET EXCITED STATE

Here we present a detailed analytical derivation of the spin relaxation of SiV^0 for an Orbach process mediated by a spin-singlet excited state. The neutral silicon vacancy center has D_{3d} symmetry with a ground spin-triplet state ($^3A_{2g}$), and the first excited singlet state is expected to be ^1E_g. The splitting between these states is unknown. At zero magnetic field, the triplet and singlet states can mix through spin-orbit coupling assisted by phonons [37–40],

$$\begin{aligned}
\left|{}^3\bar{A}_{2g}^{m_s=0}\right\rangle &= \left|{}^3A_{2g}^{m_s=0}\right\rangle + t_0^0\left|{}^1E_g\right\rangle,\\
\left|{}^3\bar{A}_{2g}^{m_s=+1}\right\rangle &= \left|{}^3A_{2g}^{m_s=+1}\right\rangle + t_{+1}^0\left|{}^1E_g\right\rangle,\\
\left|{}^3\bar{A}_{2g}^{m_s=-1}\right\rangle &= \left|{}^3A_{2g}^{m_s=-1}\right\rangle + t_{-1}^0\left|{}^1E_g\right\rangle,\\
|{}^1\bar{E}_g\rangle &= |{}^1E_g\rangle + \sum_{m_s} t_{m_s}^0\left|{}^3A_{2g}^{m_s}\right\rangle, \qquad \text{(G1)}
\end{aligned}$$

where $t_{m_s}^0$ are state mixing coefficients. In the main text we refer to them as overlap parameters that connect the singlet and triplet subspaces since $t_{m_s}^0 = \langle {}^3\bar{A}_{2g}^{m_s}|{}^1\bar{E}_g\rangle$. The $t_{m_s}^0$ coefficients arise from spin-orbit coupling and thus depend only on the orbital symmetry of the involved zero-field states, which is independent of the applied magnetic field.

The triplet eigenstates in the presence of a magnetic field can be found using a Wigner rotation to transform the eigenstates of the zero-field splitting term from the molecular frame to the laboratory frame (the frame in which the Zeeman interaction is diagonal). This model assumes that in a magnetic field the eigenstates of the spin Hamiltonian have mostly Zeeman character and the zero-field splitting term can be neglected ($g\mu_B B/h \gg D$). A general rotation R can be expressed in terms of Euler angles,

$$R\,(\alpha,\beta,\gamma) = R_{\hat{z}}(\gamma)R_{\hat{n}}(\beta)R_{\hat{z}}(\alpha), \qquad \text{(G2)}$$

where $\vec{\Omega} = (\alpha,\beta,\gamma)$ is the set of Euler angles following the "passive" convention. Under this rotation the irreducible tensors in the spin Hamiltonian $T_{J,m}$ transform to $\rho_{J,m}$ as

$$\begin{aligned}
\rho_{J,m} &= R(\alpha,\beta,\gamma)T_{J,m}R^{-1}(\alpha,\beta,\gamma)\\
&= \sum_{m'} D_{m',m}^{J}(\alpha,\beta,\gamma)T_{J,m'}, \qquad \text{(G3)}
\end{aligned}$$

where $D_{m',m}^{J}(\Omega)$ is the Wigner matrix of rank J. The elements of this matrix are as follows:

$$D_{m',m}^{J}(\alpha,\beta,\gamma) = \exp(-im'\alpha)d_{m',m}^{J}(\beta)\exp(-im\gamma), \qquad \text{(G4)}$$

with

$$d_{m',m}^{J}(\beta) = \int_{\theta,\phi} d\Omega\, Y_{Jm'}^{*}(\theta,\phi)e^{-(i/\hbar)\beta J_{\hat{n}}}Y_{Jm}(\theta,\phi), \qquad \text{(G5)}$$

where $Y_{Jm'}(\theta,\phi)$'s are the standard spherical harmonic functions and $J_{\hat{n}}$ is the component of the total angular momentum along $\hat{n} \parallel \langle 110\rangle$. Then for $J = S = 1$,

$$D_{m',m}^{S=1}(\alpha,\beta,\gamma) = \begin{pmatrix} \frac{1+\cos(\beta)}{2}e^{-i(\alpha+\gamma)} & -\frac{1}{\sqrt{2}}\sin(\beta)e^{-i\alpha} & \frac{1-\cos(\beta)}{2}e^{-i(\alpha-\gamma)}\\ \frac{1}{\sqrt{2}}\sin(\beta)e^{-i\gamma} & \cos(\beta) & -\frac{1}{\sqrt{2}}\sin(\beta)e^{i\gamma}\\ \frac{1-\cos(\beta)}{2}e^{i(\alpha-\gamma)} & \frac{1}{\sqrt{2}}\sin(\beta)e^{i\alpha} & \frac{1+\cos(\beta)}{2}e^{i(\alpha+\gamma)} \end{pmatrix}. \qquad \text{(G6)}$$

If we specifically define R as the rotation away from $\langle 111\rangle$ about the $\langle 110\rangle$ axis so that $\alpha = \varphi$, $\beta = \theta$, and $\gamma = 0^\circ$ define the orientation of the magnetic field, the mixing of the transition amplitudes is given by

$$t_{m'} = \sum_{m} D_{m',m}^{S=1}(\varphi,\theta,0)t_m^0. \qquad \text{(G7)}$$

From this we obtain the transition rates ($|t_m|^2$) by invoking the random-phase approximation to neglect the cross terms (averaging over φ). The physical origin of the random-phase approximation can arise from taking an ensemble average over a bath of phonons that randomly induce transitions to the excited state through spin-orbit coupling. The result is as follows:

$$|t_{m'}|^2 = \sum_{m} \left\langle \left| D_{m',m}^{S=1}(\varphi,\theta,0)\right|^2\right\rangle_{\varphi} |t_m^0|^2, \qquad \text{(G8)}$$

where

$$\langle |D^{S=1}_{m',m}(\varphi,\theta,0)|^2\rangle_\varphi = \begin{pmatrix} \cos^4(\theta/2) & \frac{1}{2}\sin^2(\theta) & \sin^4(\theta/2) \\ \frac{1}{2}\sin^2(\theta) & \cos^2(\theta) & \frac{1}{2}\sin^2(\theta) \\ \sin^4(\theta/2) & \frac{1}{2}\sin^2(\theta) & \cos^4(\theta/2) \end{pmatrix}. \tag{G9}$$

In the main text, Eq. (3) for the overlap coefficients in the presence of an off-axis magnetic field is obtained by substituting Eq. (G9) into Eq. (G8).

Next, the transition rate matrix [Eq. (G9)] can be used to model the spin-relaxation processes for $S = 1$ where the populations $\boldsymbol{P} = (P_{-1}, P_0, P_{+1})$ evolve according to

$$\frac{d\boldsymbol{P}(t)}{dt} = \tilde{R}\boldsymbol{P}(t), \tag{G10}$$

where the rate matrix $\tilde{R}$ is given by

$$\tilde{R}_{m,m'} = C(1-\delta_{m,m'})\mu^{m-m'}|t_m|^2|t_{m'}|^2 - C\delta_{m,m'}\left(\sum_{m''\neq m}|t_m|^2|t_{m''}|^2\mu^{m''-m}\right), \tag{G11}$$

where $\delta_{m,m'}$ is the Kronecker δ function and $\mu = \exp(hf/kT)$ is the Boltzmann factor at $T = 30$ K and $f = 9.7$ GHz. Assuming that $|t^0_{+1}| = |t^0_{-1}|$ and $\mu = 1 (hf \ll kT)$, this results in two distinct rate eigenvalues λ_1 and λ_2 corresponding to $T_{1,a} = \lambda_1^{-1}e^{-E_a/kT}$ and $T_{1,b} = \lambda_2^{-1}e^{-E_a/kT}$,

$$T_{1,a} = \frac{2e^{-E_a/kT}}{3C|t_0|^2(|t_{+1}|^2+|t_{-1}|^2)}$$
$$T_{1,b} = \frac{e^{-E_a/kT}}{C|t_{-1}|^2(2|t_{+1}|^2+|t_0|^2)}. \tag{G12}$$

Equations (G12) were used to simulate the angular dependence of T_1 as a function of $|t_0|/|t_{\pm1}|$ in Figs. 3(a) and 4(b). If we assume that $|t^0_0| \gg |t^0_{\pm1}|$ then Eqs. (G12) reduce to Eqs. (5).

APPENDIX H: MODEL FOR SPIN RELAXATION: ORBACH PROCESS WITH A TRIPLET EXCITED STATE

The excited state can also be a spin-triplet state, such as a quasilocalized vibronic mode or a low lying electronic state. For this model we define two $S = 1$ spin Hamiltonians for the ground state ($\hat{H}_g$) and excited state ($\hat{H}_e$) that differ only in their zero-field splitting tensors ($\tilde{D}_g \neq \tilde{D}_e$),

$$\hat{H}_g = \hat{\boldsymbol{S}}^\dagger\tilde{D}_g\hat{\boldsymbol{S}} + \mu_B\hat{\boldsymbol{S}}^\dagger\tilde{g}\boldsymbol{B} \quad \hat{H}_e = \hat{\boldsymbol{S}}^\dagger\tilde{D}_e\hat{\boldsymbol{S}} + \mu_B\hat{\boldsymbol{S}}^\dagger\tilde{g}\boldsymbol{B}, \tag{H1}$$

with eigenstates $|m_s\rangle_g$ and $|n_s\rangle_e$, respectively. The rate matrix describing the spin relaxation is given by

$$R_{m,m'} = C(1-\delta_{m,m'})\sum_n |{}_g\langle m|n\rangle_{ee}\langle n|m'\rangle_g|^2\mu^{m-m'} - C\delta_{m,m'}\left(\sum_{m''\neq m}\mu^{m''-m}\sum_n|{}_g\langle m''|n\rangle_{ee}\langle n|m\rangle_g|^2\right). \tag{H2}$$

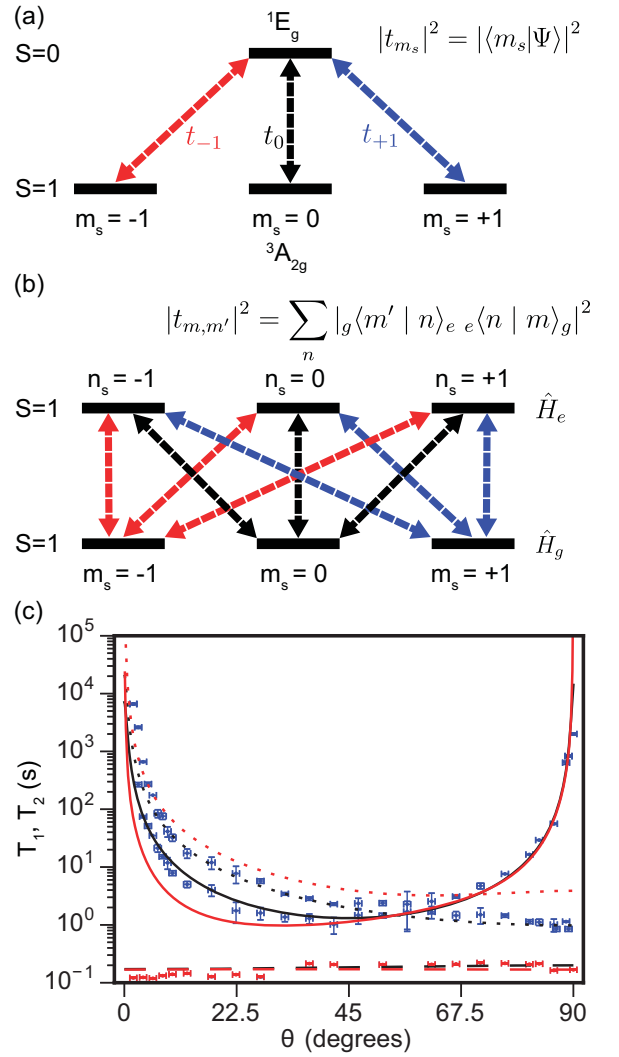

FIG. 10. (a) Model for the Orbach process of SiV^0 with a singlet excited state. The transition rates ($|t_{m_s}|^2$) are determined by spin-orbit coupling and depend on the overlap between the electronic wave functions of the ground triplet state and the excited singlet state. (b) Model for the Orbach process of SiV^0 with a triplet excited state. The transition rates between the ground-state spin sublevels depend on the overlap between the spin eigenstates of the ground state and the excited state and must be summed over all spin sublevels in the excited state. (c) T_1 and T_2 orientation dependence from Fig. 3(a), plotted against calculated fits from the singlet (black) and triplet (red) Orbach models: $T_{1,a}$ (solid line), $T_{1,b}$ (dashed line), and T_2 (long dashed line). The singlet model fit assumes $|t^0_0/t^0_{\pm1}| = 125$. The triplet model fit assumes a coaxial excited state ZFS tensor with $D_e = 5$ GHz.

In the triplet model spin flips can occur through any of the three spin sublevels of the excited state [Fig. 10(b)], increasing the complexity of the rate matrix. Spin relaxation arises from the overlap between the eigenstates of the two triplet states, and slight variations in the character of the states become important. Thus the zero-field splitting terms for both the ground state and the excited state cannot be neglected when calculating the triplet state overlap coefficients and the rate matrix ($R_{m,m'}$). For these reasons the analytical solution for

the Orbach model with a triplet excited state is not compact, and instead we numerically simulate the spin relaxation by diagonalizing the rate matrix Eq. (H2).

In general, $\tilde{D}_e$ can differ from $\tilde{D}_g$ in its quantization axis, its magnitude of the axial component, or its magnitude of the rhombicity parameter. In the case where the quantization axis of the excited state is not aligned with the quantization axis of the ground state (e.g., due to an E-type quasilocalized vibronic mode that breaks D_{3d} symmetry), the resulting orientation dependence qualitatively disagrees with the T_1 data. The same disagreement was found to be true for the case where rhombicity was introduced into the excited-state spin Hamiltonian. However, the orientation dependence of T_1 can be partially reproduced by assuming that $\tilde{D}_e$ is axial (no rhombicity) and coaxial with the ground-state $\tilde{D}_g$ thus preserving D_{3d} symmetry. Focusing on just fitting the T_1 orientation dependence (ignoring T_2), the closest fit to the T_1 data was found with $D_e = 1$ GHz. However, this excited-state zero-field splitting tensor predicts that $T_2 \sim 100$ ns, which is inconsistent with the measured values. As described in the main text, the Zeeman energy is high, and in order to reproduce the T_2 data, D_e needs to be comparable to the Zeeman energy, and the T_2 data are reproduced best by the triplet model when $D_e \approx 5$–7 GHz (Fig. 11). The simulated orientation dependence of T_1 for this excited-state zero-field splitting is qualitatively similar to the data but lies outside of the error bars for both time constants [Fig. 10(c)]. Furthermore, such a large difference in zero-field splitting between the ground and the excited states is unlikely.

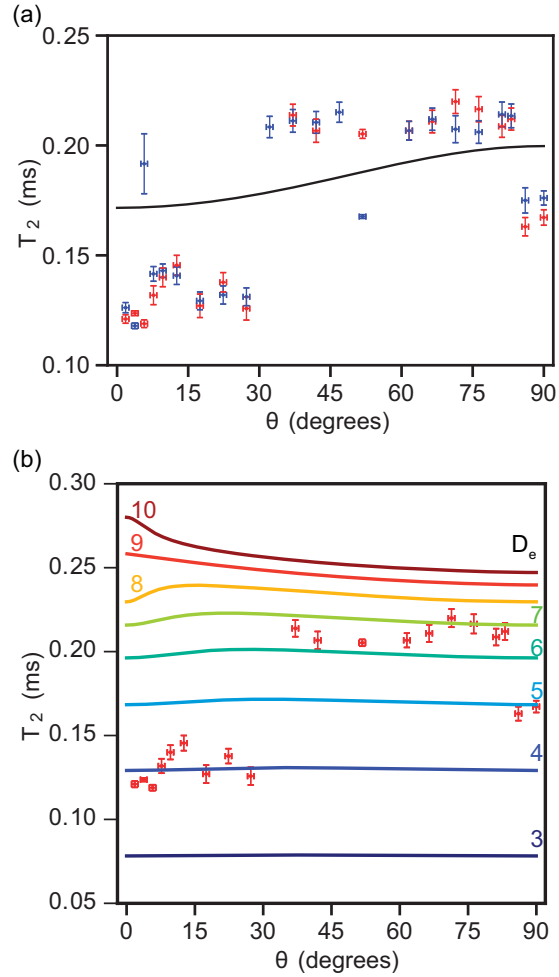

FIG. 11. Orientation dependence of the SiV^0 electron spin coherence time T_2 [replotted from Fig. 3(a)]. (a) Predicted orientation dependence using an Orbach model with a singlet excited state [black curve, Eq. (I1)] with no free parameters. Measurements were performed on both the $m_s = 0 \leftrightarrow +1$ transition (red points) and the $m_s = -1 \leftrightarrow 0$ transition (blue points) at each orientation. (b) Predicted orientation dependence of an Orbach model with a triplet excited state. The simulated curves are shown for several values of D_e (labeled in units of gigahertz).

APPENDIX I: ORIENTATION DEPENDENCE OF T_2

Our model for the Orbach process predicts a weak orientation dependence of T_2. The orientation dependence fits shown in Fig. 3(a) utilize the same overlap amplitudes $(t_0^0, t_{\pm1}^0)$ to explain both T_1 and T_2. The actual expression used in fitting the T_2 dependence in Fig. 3(a) is given by

$$\frac{1}{T_{2,0\leftrightarrow\pm1}} = \frac{1}{3}C\left(|t_0^0|^2 + 2|t_{\pm1}^0|^2\right)\left(|t_0|^2 + |t_{\pm1}|^2\right) + \frac{1}{T_{2(ID)}} + \frac{1}{T_{2(SD)}}, \tag{I1}$$

which in addition to the Orbach process also includes instantaneous diffusion and ^{13}C spectral diffusion mechanisms. We used $T_{2(ID)} = 0.319$ and $T_{2(SD)} = 0.95$ ms in these simulations.

The orientation dependence of T_2 is shown in Fig. 11 with the simulated fits according to the singlet [Fig. 11(a)] and triplet [Fig. 11(b)] models using the $t_{m_s}^0$ and C parameters determined from the T_1 data. The singlet model has no other free-fitting parameters, and we plot Eq. (I1) for the singlet model assuming that $|t_0^0/t_{\pm1}^0| = 125$ as determined from the fit of the T_1 orientation dependence [Fig. 3(a)]. The singlet model predicts the magnitude of T_2 with reasonable accuracy.

The triplet model has four free parameters, two angles that set the quantization axis of the excited state, the axial part of the zero-field splitting tensor, and the rhombic part of the zero-field splitting tensor. We only consider the case where the zero-field splitting tensor of the excited state is axial and aligned with the symmetry axis of the defect since this is the case that best produces the measured T_1 orientation dependence [Fig. 10(c)]. The dependence for several values of D_e is shown, and the best fit occurs with $D_e \approx 5$–7 GHz. Alternatively, if the spin does not fully decohere through a single cycle through the excited

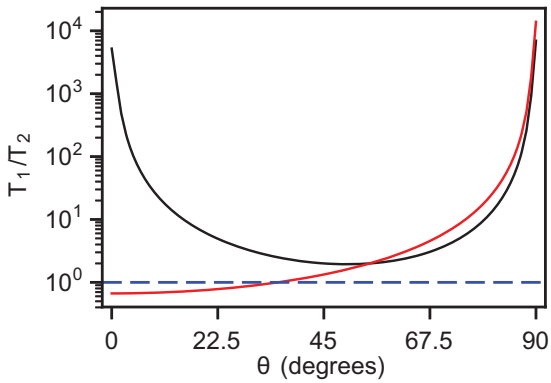

FIG. 12. Simulated orientation dependence of T_1/T_2 for the Orbach process at 30 K showing the $m_s = 0 \leftrightarrow +1$ (black curve) and $m_s = -1 \leftrightarrow +1$ (red curve) coherence times compared to $T_{1,a}$. The dashed blue line marks where $T_1 = T_2$, and only the $m_s = -1 \leftrightarrow +1$ curve dips below this, achieving the condition $T_1/T_2 < 1$.

state, the magnitude of T_2 can be larger than the simulated values.

APPENDIX J: DOUBLE-QUANTUM COHERENCE TIME

The Orbach process affects the double-quantum transition ($m_s = -1 \leftrightarrow +1$) through the overlap parameters t_{+1}, t_{-1}, and from the anisotropy of T_1 (Fig. 3), we know that $|t^0_{+1}|, |t^0_{-1}| \ll |t^0_0|$. It follows that $\frac{1}{T_{2,-1\leftrightarrow+1}} \propto |t^0_{-1}| + |t^0_{+1}| \ll |t^0_{\pm1}| + |t^0_0| = \frac{1}{T_{2,\pm1\leftrightarrow0}}$ so that the double-quantum coherence time should be longer at the zero field or with the magnetic field aligned along the defect axis. Moreover for small angles of the magnetic field the double-quantum coherence time can be longer than the single-quantum T_1 time, even when the single-quantum coherence time is much shorter (Fig. 12).

[1] G. Balasubramanian, I. Y. Chan, R. Kolesov, M. Al-Hmoud, J. Tisler, C. Shin, C. Kim, A. Wojcik, P. R. Hemmer, A. Krueger, T. Hanke, A. Leitenstorfer, R. Bratschitsch, F. Jelezko, and J. Wrachtrup, Nanoscale imaging magnetometry with diamond spins under ambient conditions, Nature (London) **455**, 648 (2008).

[2] T. Gaebel, M. Domhan, I. Popa, C. Wittmann, P. Neumann, F. Jelezko, J. R. Rabeau, N. Stavrias, A. D. Greentree, S. Prawer, J. Meijer, J. Twamley, P. R. Hemmer, and J. Wrachtrup, Room-temperature coherent coupling of single spins in diamond, Nat. Phys. **2**, 408 (2006).

[3] M. V. Gurudev Dutt, L. Childress, L. Jiang, E. Togan, J. Maze, F. Jelezko, A. S. Zibrov, P. R. Hemmer, and M. D. Lukin, Quantum register based on individual electronic and nuclear spin qubits in diamond, Science **316**, 1312 (2007).

[4] P. C. Maurer, G. Kucsko, C. Latta, L. Jiang, N. Y. Yao, S. D. Bennett, F. Pastawski, D. Hunger, N. Chisholm, M. Markham, D. J. Twitchen, J. I. Cirac, and M. D. Lukin, Room-temperature quantum bit memory exceeding one second, Science **336**, 1283 (2012).

[5] F. Dolde, I. Jakobi, B. Naydenov, N. Zhao, S. Pezzagna, C. Trautmann, J. Meijer, P. Neumann, F. Jelezko, and J. Wrachtrup, Room-temperature entanglement between single defect spins in diamond, Nat. Phys. **9**, 139 (2013).

[6] E. Togan, Y. Chu, A. S. Trifonov, L. Jiang, J. Maze, L. Childress, M. V. G. Dutt, A. S. Sorensen, P. R. Hemmer, A. S. Zibrov, and M. D. Lukin, Quantum entanglement between an optical photon and a solid-state spin qubit, Nature (London) **466**, 730 (2010).

[7] W. Pfaff, B. J. Hensen, H. Bernien, S. B. van Dam, M. S. Blok, T. H. Taminiau, M. J. Tiggelman, R. N. Schouten, M. Markham, D. J. Twitchen, and R. Hanson, Unconditional quantum teleportation between distant solid-state quantum bits, Science **345**, 532 (2014).

[8] B. Hensen, H. Bernien, A. E. Dreau, A. Reiserer, N. Kalb, M. S. Blok, J. Ruitenberg, R. F. L. Vermeulen, R. N. Schouten, C. Abellan, W. Amaya, V. Pruneri, M. W. Mitchell, M. Markham, D. J. Twitchen, D. Elkouss, S. Wehner, T. H. Taminiau, and R. Hanson, Loophole-free bell inequality violation using electron spins separated by 1.3 kilometres, Nature (London) **526**, 682 (2015).

[9] K. D. Jahnke, A. Sipahigil, J. M. Binder, M. W. Doherty, M. Metsch, L. J. Rogers, N. B. Manson, M. D. Lukin, and F. Jelezko, Electron-phonon processes of the silicon-vacancy center in diamond, New J. Phys. **17**, 043011 (2015).

[10] A. Sipahigil, R. E. Evans, D. D. Sukachev, M. J. Burek, J. Borregaard, M. K. Bhaskar, C. T. Nguyen, J. L. Pacheco, H. A. Atikian, C. Meuwly, R. M. Camacho, F. Jelezko, E. Bielejec, H. Park, M. Lončar, and M. D. Lukin, An integrated diamond nanophotonics platform for quantum-optical networks, Science **354**, 847 (2016).

[11] B. C. Rose, D. Huang, Z.-H. Zhang, A. M. Tyryshkin, S. Sangtawesin, S. Srinivasan, L. Loudin, M. L. Markham, A. M. Edmonds, D. J. Twitchen, S. A. Lyon, and N. P. de Leon, Observation of an environmentally insensitive solid-state spin defect in diamond, Science **361**, 60 (2018).

[12] B. L. Green, S. Mottishaw, B. G. Breeze, A. M. Edmonds, U. F. S. D'Haenens-Johansson, M. W. Doherty, S. D. Williams, D. J. Twitchen, and M. E. Newton, Neutral Silicon-Vacancy Center in Diamond: Spin Polarization and Lifetimes, Phys. Rev. Lett. **119**, 096402 (2017).

[13] R. Orbach, Spin-lattice relaxation in rare-earth salts, Proc. R. Soc. London A **264**, 458 (1961).

[14] R. Orbach and H. J. Stapleton, in *Electron Paramagnetic Resonance*, edited by S. Geschwind (Plenum, New York, 1972), Chap. 2 .

[15] K. N. Shrivastava, Theory of spin-lattice relaxation, Phys. Status Solidi B **117**, 437 (1983).

[16] L. J. Rogers, K. D. Jahnke, M. H. Metsch, A. Sipahigil, J. M. Binder, T. Teraji, H. Sumiya, J. Isoya, M. D. Lukin, P. Hemmer, and F. Jelezko, All-Optical Initialization, Readout, and Coherent Preparation of Single Silicon-Vacancy Spins in Diamond, Phys. Rev. Lett. **113**, 263602 (2014).

[17] A. M. Zaitsev, Vibronic spectra of impurity-related optical centers in diamond, Phys. Rev. B **61**, 12909 (2000).

[18] A. M. Edmonds, M. E. Newton, P. M. Martineau, D. J. Twitchen, and S. D. Williams, Electron paramagnetic resonance studies of silicon-related defects in diamond, Phys. Rev. B **77**, 245205 (2008).

[19] F. J. Rosenbaum, Dielectric cavity resonator for ESR experiments, Rev. Sci. Instrum. **35**, 1550 (1964).

[20] A. Schweiger and G. Jeschke, *Principles of Pulse Electron Paramagnetic Resonance* (Oxford University Press, Oxford, 2001) .

[21] A. M. Tyryshkin, S. Tojo, J. J. L. Morton, H. Riemann, N. V. Abrosimov, P. Becker, H.-J. Pohl, T. Schenkel, M. L. W. Thewalt, K. M. Itoh, and S. A. Lyon, Electron spin coherence exceeding seconds in high-purity silicon, Nature Mater. **11**, 143 (2012).

[22] A. Jarmola, V. M. Acosta, K. Jensen, S. Chemerisov, and D. Budker, Temperature- and Magnetic-Field-Dependent Longitudinal Spin Relaxation in Nitrogen-Vacancy Ensembles in Diamond, Phys. Rev. Lett. **108**, 197601 (2012).

[23] C. A. Van't Hof and J. Schmidt, Zero-field magnetic resonance in the photo-excited triplet state of p-benzoquinone under the influence of vibronic relaxation, Chem. Phys. Lett. **42**, 73 (1976).

[24] P. Kehayias, M. W. Doherty, D. English, R. Fischer, A. Jarmola, K. Jensen, N. Leefer, P. Hemmer, N. B. Manson, and D. Budker, Infrared absorption band and vibronic structure of the nitrogen-vacancy center in diamond, Phys. Rev. B **88**, 165202 (2013).

[25] V. M. Huxter, T. A. A. Oliver, D. Budker, and G. R. Fleming, Vibrational and electronic dynamics of nitrogen-vacancy centres in diamond revealed by two-dimensional ultrafast spectroscopy, Nat. Phys. **9**, 744 (2013).

[26] A. Dräbenstedt, L. Fleury, C. Tietz, F. Jelezko, S. Kilin, A. Nizovtzev, and J. Wrachtrup, Low-temperature microscopy and spectroscopy on single defect centers in diamond, Phys. Rev. B **60**, 11503 (1999).

[27] F. Jelezko and J. Wrachtrup, Single defect centres in diamond: A review, Phys. Status Solidi A **203**, 3207 (2006).

[28] M. Mrózek, D. Rudnicki, P. Kehayias, A. Jarmola, D. Budker, and W. Gawlik, Longitudinal spin relaxation in nitrogen-vacancy ensembles in diamond, EPJ Quantum Technology **2**, 22 (2015).

[29] J. N. Becker, B. Pingault, D. Groß, M. Gündoğan, N. Kukharchyk, M. Markham, A. Edmonds, M. Atatüre, P. Bushev, and C. Becher, All-Optical Control of the Silicon-Vacancy Spin in Diamond at Millikelvin Temperatures, Phys. Rev. Lett. **120**, 053603 (2018).

[30] D. D. Sukachev, A. Sipahigil, C. T. Nguyen, M. K. Bhaskar, R. E. Evans, F. Jelezko, and M. D. Lukin, The Silicon-Vacancy Spin Qubit in Diamond: Quantum Memory Exceeding Ten Milliseconds and Single-Shot State Readout, Phys. Rev. Lett. **119**, 223602 (2017).

[31] B. A. Myers, A. Ariyaratne, and A. C. Bleszynski Jayich, Double-Quantum Spin-Relaxation Limits to Coherence of Near-Surface Nitrogen-Vacancy Centers, Phys. Rev. Lett. **118**, 197201 (2017).

[32] J. R. Klauder and P. W. Anderson, Spectral diffusion decay in spin resonance experiments, Phys. Rev. **125**, 912 (1962).

[33] A. M. Edmonds, Magnetic resonance studies of point defects in single crystal diamond, Ph.D. thesis, University of Warwick, 2008.

[34] W. B. Mims, Phase memory in electron spin echoes, lattice relaxation effects in CaWO_{4}: Er, Ce, Mn, Phys. Rev. **168**, 370 (1968).

[35] K. M. Salikhov, S. A. Dzuba, and A. M. Raitsimring, The theory of electron spin-echo signal decay resulting from dipole-dipole interactions between paramagnetic centers in solids, J. Magn. Reson. **42**, 255 (1981).

[36] S. Meiboom and D. Gill, Modified spin-echo method for measuring nuclear relaxation times, Rev. Sci. Instrum. **29**, 688 (1958).

[37] M. L. Goldman, A. Sipahigil, M. W. Doherty, N. Y. Yao, S. D. Bennett, M. Markham, D. J. Twitchen, N. B. Manson, A. Kubanek, and M. D. Lukin, Phonon-Induced Population Dynamics and Intersystem Crossing in Nitrogen-Vacancy Centers, Phys. Rev. Lett. **114**, 145502 (2015).

[38] M. L. Goldman, M. W. Doherty, A. Sipahigil, N. Y. Yao, S. D. Bennett, N. B. Manson, A. Kubanek, and M. D. Lukin, State-selective intersystem crossing in nitrogen-vacancy centers, Phys. Rev. B **91**, 165201 (2015).

[39] G. Thiering and A. Gali, Ab initio calculation of spin-orbit coupling for an NV center in diamond exhibiting dynamic Jahn-Teller effect, Phys. Rev. B **96**, 081115 (2017).

[40] M. W. Doherty, N. B. Manson, P. Delaney, and L.C.L. Hollenberg, The negatively charged nitrogen-vacancy center in diamond: The electronic solution, New J. Phys. **13**, 025019 (2011).